Steel and Composite Structures, *Vol. 28, No. 6 (2018) 691-708*
DOI: https://doi.org/10.12989/scs.2018.28.6.691

Direct displacement based design of hybrid passive resistive truss girder frames

Amir Hamzeh Shaghaghian [1a], Morteza Raissi Dehkordi [*1] and Mahdi Eghbali [2b]

[1] *School of Civil Engineering, Iran University of Science and Technology (IUST), Tehran, Iran*
[2] *Department of Civil Engineering, Faculty of Engineering, University of Zanjan, Zanjan, Iran*

(*Received July 12, 2017, Revised November 1, 2017, Accepted July 31, 2018*)

Abstract. An innovative Hybrid Passive Resistive configuration for Truss Girder Frames (HPR-TGFs) is introduced in the present study. The proposed system is principally consisting of Fluid Viscous Dampers (FVDs) and Buckling Restrained Braces (BRBs) as its seismic resistive components. Concurrent utilization of these devices will develop an efficient energy dissipating mechanism which is able to mitigate lateral displacements as well as the base shear, simultaneously. However, under certain circumstances which the presence of FVDs might not be essential, the proposed configuration has the potential to incorporate double BRBs in order to achieve the redundancy of alternative load bearing paths. This study is extending the modern Direct Displacement Based Design (DDBD) procedure as the design methodology for HPR-TGF systems. Based on a series of nonlinear time history analysis, it is demonstrated that the design outcomes are almost identical to the pre-assumed design criteria. This implies that the ultimate characteristics of HPR-TGFs such as lateral stiffness and inter-story drifts are well-proportioned through the proposed design procedure.

Keywords: truss girder frames; hybrid passive resistance; direct displacement based design; energy dissipating devices; V-shaped link; bolted hinges

1. Introduction

As required by ASCE7 (2010) Section 11.1.1, the specified earthquake loads are based upon post-elastic energy dissipation in the structure. In the scope of steel moment frames, the plastic hinging of the beams is responsible for providing the inelastic performance of the system. Accordingly, Erfani *et al*. (2012) have proven that the presence of web openings will protect the beam-column connections against inelastic deformations while the overall reduction of stiffness is negligible. Thus, the utilization of trusses instead of massive plate-girders is a wise solution to improve seismic characteristics of moment frames. In this regard, special truss girders are well-qualified to possess efficient detailing for controlled inelastic deformations. Truss moment frames are also providing higher lateral stiffness with relatively less weight in comparison to the plate-girder moment frames. Early experimental and analytical studies by Goel and Itani (1994a) were a beginning to clarify the characteristics of these framing systems. They declared that Ordinary Truss Moment Frames (OTMFs) show very poor hysteretic behavior under cyclic loading. Hence, they've proposed the fundamental concept of "ductile truss girders". The most primary form of these girders consists of X-diagonal braced panels in the middle of trusses (Goel and Itani 1994b). These braced panels are designed to dissipate energy through buckling and yielding of X-diagonals. Since the diagonal components might cause some obstructions for the ductworks passing through trusses, Basha and Goel (1995) have proposed another type of ductile truss girders with a "Vierendeel" special segment. This configuration can provide more open space in the middle segment of trusses, as well as offering fuller and non-degrading hysteretic loops. Later on, Chao and Goel (2008) have alternated the elastic design approach carried out for special truss moment frames by a more efficient performance based plastic design procedure. However, all of the above-mentioned structural configurations and their design methodologies are merely relying on the inherent capacity of structure to dissipate seismic input energy which is not proper for modern earthquake engineering.

In the scope of truss girder frames, Pekcan *et al*. (2009) were the first ones to propose a configuration that is aimed to maintain structural components in the elastic range and enforce inelastic deformations in special mechanical devices considered for the dissipation of earthquake energy. Their idea has generally been followed by various researchers with some newfound configurations. For example, Wongpakdee *et al*. (2014) proposed an innovative arrangement which uses Buckling Restrained Braces (BRBs) as knee bracing for truss girder frames. Another possible seismic resistive configuration is to form bending performance in the truss girders. Heidari and Gharehbaghi (2015) have practically applied this concept by embedding double BRBs on the either side of trusses. Moreover, there

∗Corresponding author, Assistant Professor,
E-mail: mraissi@iust.ac.ir
[a] M.Sc., E-mail: a_shaghaghian@civileng.iust.ac.ir
[b] Assistant Professor, E-mail: eghbali@znu.ac.ir

http://www.techno-press.org/?journal=scs&subpage=6
ISSN: 1229-9367 (Print), 1598-6233 (Online)

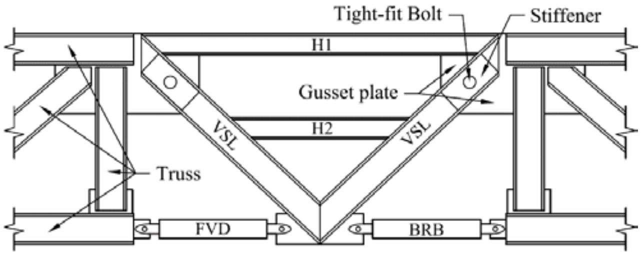

Fig. 1 Special segment with multi phase energy dissipation

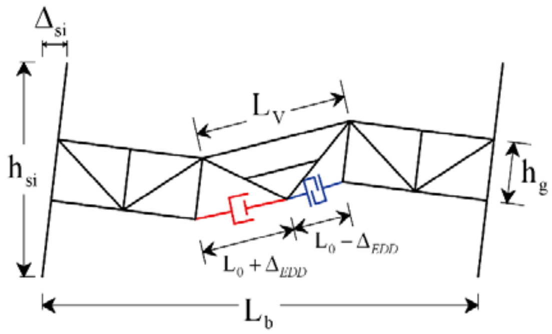

Fig. 2 The exaggerated deformation of a hybrid passive resistive truss girder

have been some efforts on incorporating viscous dampers for rehabilitation of existing truss moment frames (Kim *et al*. 2016) and hence developing a procedure for utilizing viscous dampers in brand-new truss girder frames would be a challenging issue. This idea which essentially requires the simultaneous utilization of different energy dissipating phases is previously proposed and successfully tested for conventional steel moment frames (Magar Patil and Jangid 2015).

This discussion is eventually leading to the concept of multi-phase energy dissipation for truss girder frames. Factual fulfillment of this idea requires a specific type of truss girder which can be achieved by embedding a rigid V-Shaped Link (VSL) in the middle segment of truss girders. Since the presence of VSL might cause a sharp kink in trusses, it's been accompanied by two horizontal components (H1 and H2 in the Fig. 1). In this study, passive Energy Dissipating Devices (EDDs) such as Fluid Viscous Dampers (FVDs) and Buckling Restrained Braces (BRBs) are utilized to form the seismic load bearing mechanism. Hence, the overall set has been named as Hybrid Passive Resistive Truss Girder Frame (HPR-TGF). On the other hand, the newly proposed configuration of HPR-TGFs requires an appropriate design process to meet the seismic demands properly. In the conventional Force-Based Design (FBD) methodologies the performance objective is confined to the ultimate and the serviceability limit states. More specifically, the design forces are based on the elastic state of the structure which will be reduced by the response modification factor. These considerations imply that the traditional FBD is accompanied with serious approximations. Accordingly, Priestley (1993) has expressed the principal necessity of alternating displacement criteria instead of strength demands in the seismic design of structures. Since lateral displacements are capable of describing the damage due to seismic events and subsequently to measure the performance of structures, the displacement based design procedure is considered as an efficient approach for the performance-based design of structures. Thus, fundamentals of the Direct Displacement Based Design (DDBD) have been introduced as a promising methodology for the next generation of building codes (Fajfar and Krawinkler 1997). The representation of performance levels in the DDBD is expressed through a quantitative value of the target drift capacity which involves directly in the design process. The detailed characteristics of this procedure for various structural systems are described in a book by Priestley *et al*. (2007). Moreover, this design methodology has been individually proposed and successfully validated for some of more specific seismic design purposes such as base isolated bridges (Amiri *et al*. 2016). Salawdeh and Goggins (2016a) have developed the DDBD procedure for concentrically braced frames and they evaluated its outcomes versus those of a conventional force-based design approach (Salawdeh and Goggins 2016b). However, despite the extensive efforts in the scope of direct displacement-based design procedure, it hasn't yet been implemented for the truss girder frames. Therefore, this study is intended to develop this procedure for the proposed HPR-TGF system. The design guidelines are presented for the comprehensive state with Fluid Viscous Dampers (FVDs) and Buckling Restrained Braces (BRBs) and the equations required for the alternative setup with double BRBs can be inferred accordingly.

2. Feasibility of practical implementation

The duty of V-shaped link in a hybrid passive resistive truss girder, as expressed by Eq. (1), is to correlate inter-story drifts at the ith story ($\theta_i = \Delta_{si}/h_{si}$ in the Fig. 2) to the deformation of Energy Dissipating Devices (EDDs) at the level under consideration (Δ_{EDD} in the Fig. 2).

$$\Delta_{EDD} = \frac{L_b \cdot h_g}{L_V} \times \theta_i \tag{1}$$

where the rest of symbols are defined with reference to the Fig. 2.

Since proper functioning of the VSL is highly depending on its connections, it is essential to provide executive details for them. The main fragments in these hinges are the bolts considered to transfer shear forces. Based on the engineering fundamentals, by considering σ_{yb} as the tensile yield strength of the bolts, then their maximum shear strength is $\sigma_{yb}/2$. Thus, the minimum bolt diameter (d) needed to withstand the ultimate resistive shear forces (F_{ri}) at the middle of trusses is expressed by Eq. (2) in which ω_v is the distributed load over the VSL length.

$$d = \sqrt{\frac{32(F_{ri} + \omega_v \cdot L_V/2)}{3\pi\sigma_{yb}}} \tag{2}$$

In addition to the diameter of bolts, other characteristics

Dimension	Required (mm)	Applied (mm)	Maximum Stress (σ_y=345MPa)	Status
Bolt diameter (d)	88.1	101.6	279 MPa	
Gusset thickness (Tg)	26.0	25.4	373 MPa	
Web thickness (Tw)	12.7	10.6	338 MPa	
Stiffener thickness (Ts)	2.0	12.7	310 MPa	

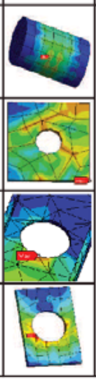

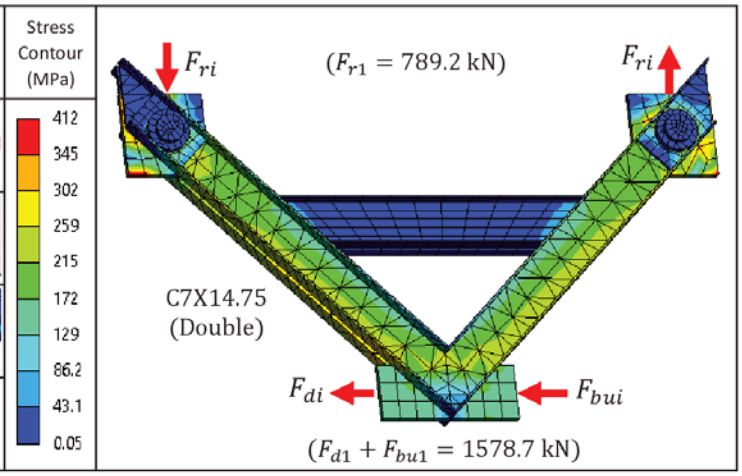

Fig. 3 von Mises stress distribution in the V-shaped link

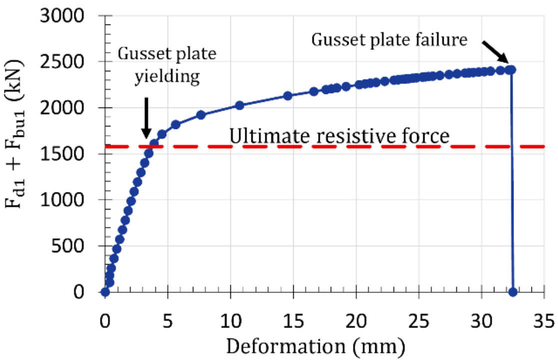

Fig. 4 Force deformation capacity of the V-shaped link

of the components involved in the bolted hinges must be specified properly. So the thickness of gusset plates is given by Eq. (3). The minimum web thickness required for the VSL channel sections is half of the thickness of its adjacent gusset plate ($t_w = t_g/2$). If the web of channel sections were thin, then stiffeners with proper thickness would be applied to meet the requirements at the attachment zones.

$$t_g = \frac{F_{ri}}{\sigma_y \cdot d} \tag{3}$$

in which σ_y is the yield strength of plates and d is as expressed by Eq. (2). The validity of the above mentioned equations has been evaluated via the ANSYS finite element program. In the practical buildings with HPR-TGF system, columns are attached to rigid floors and hence the top vertices of each VSL wouldn't get closer or go farther ($L_V = constant$). This implies that the upper horizontal component of the VSL (H1 in the Fig. 1) doesn't participate in its dynamic resistance and thus it hasn't been included in the evaluation. According to the Finite Element Analysis (FEA) results in the Fig. 3, it is evident that even the lower horizontal component doesn't get a significant amount of stresses. However, the presence of these components is firstly for providing gravitational load bearing capability (H1 in the Fig. 1) and secondly for enhancing the rigidity of the VSL by confining its out-of-plane deformations (H2 in the Fig. 1). The FEA example in the Fig. 3 is carried out for a general condition in which the shear resistive force is $F_{r1} = 789.2$ kN. The differences among "Applied dimensions" and "Required dimensions" are due to the executive restrictions. The FEA results demonstrate that no considerable stress concentration was formed and hence the corresponding equations are well characterizing the boundary conditions. Furthermore, the force-deformation curve plotted in the Fig. 4 affirms that the behavior of the VSL and its connections is perfectly linear up to the ultimate resistive force of EDDs.

3. Developing the DDBD for HPR-TGF systems

A schematic representation of the steps followed to conduct a direct displacement based design approach for HPR-TGF has been depicted in the Fig. 5. In this method, an equivalent structure which encompasses the characteristics of the main HPR-TGF system is chosen to obtain seismic demands. A more detailed overview of these steps is presented in the Fig. 6. This methodology directly accounts for the inter-story drift capacity (θ_c) as the starting step of the design process. The utilization of an inelastic distribution of lateral forces in this study has caused a series of trial and errors in the estimation of the effective period. This process is shown as an iteration loop in the Fig. 6. The presence of this loop is not contrasted with the principles of the DDBD and it converges very quickly. However, the concept of substitute structure by Shibata and Sozen (1976) is regarded as the next step of the design procedure. The substitution of HPR-TGF which has multi degrees of freedom (Fig. 5(a)) by a linear Single Degree Of Freedom (SDOF) structure is shown in the Fig. 5(b). Afterward, an equivalent viscous damping is attributed to the SDOF and then with the aid of a properly damped displacement response spectrum (Fig. 5(c)), the effective period will be estimated. Finally, with reference to Fig. 5(d), the effective stiffness and the design base shear, as expressed by Eqs. (4) and (5), can be inferred directly.

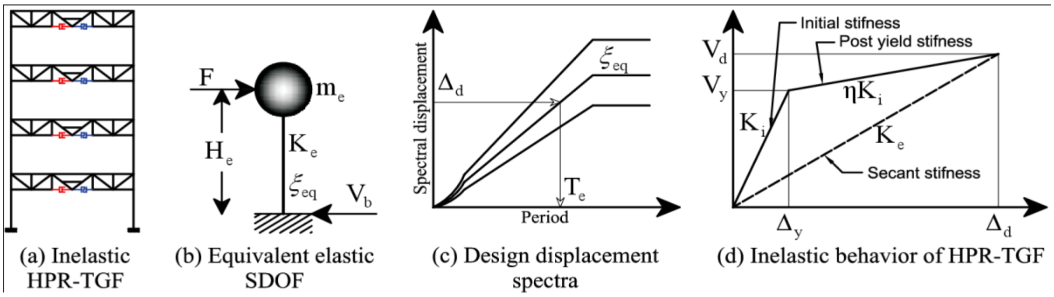

Fig. 5 Design steps for the direct displacement based method

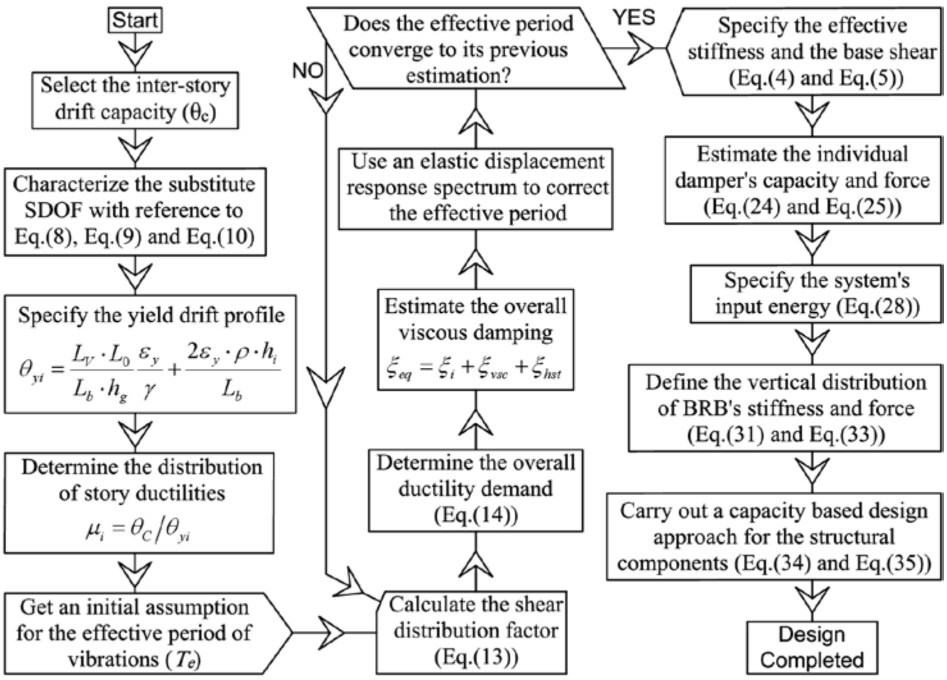

Fig. 6 Summary of the design procedure for HPR-TGF systems

$$K_e = 4\pi^2 \times \frac{m_e}{{T_e}^2} \tag{4}$$

$$V_d = K_e \times \ \Delta_d \tag{5}$$

where m_e is the effective mass, T_e is the effective period and Δ_d is the design displacement.

3.1 Ultimate drift profile

As a brief discussion on the possible methods of considering lateral sway characteristics of the structure, the theory of plastic collapse mechanism by Mazzolani and Piluso (1996) has been evaluated versus a novel approach proposed by Della Corte (2006). In order to conduct an analysis in accordance to the plastic mechanism of structures, the ultimate displaced shape is needed for the estimation of the base shear. Therefore, Priestley *et al*. (2007) have provided drift profiles for some of the well-known structural systems. These profiles are calibrated based on the statistical results of the frames. It is evident that in this method the design outcomes are highly dependent on the precision of the drift profile. On the other hand, the theory of controlling collapse mechanism for steel frames by Della Corte (2006) can intentionally dictate the formation of desirable drift profile as a sequence of the design process. This method is applied for HPR-TGFs and thus the structural elements would be wisely proportioned to exhibit a pre-defined lateral displacement profile. In order to facilitate the design procedure, an ultimately linear drift profile is chosen for HPR-TGF systems. Accordingly, the axial deformation of columns as well as the energy dissipating devices are participated in the equation of lateral displacements (Eq. (6)). The first term in Eq. (6) stands for the contribution of BRB deformations on the drift profile (Fig. 7(a)) while the second term (Fig. 7(b)) represents the axial deformation of columns at the story under consideration and also its lower stories.

$$\theta_i = \frac{L_V \cdot L_0}{L_b \cdot h_g} \cdot \frac{\mu_{bi} \cdot \varepsilon_y}{\gamma} + \frac{2\varepsilon_y}{L_b} \cdot \sum_{j=1}^{j=i} \rho_j \cdot h_{sj} \tag{6}$$

This equation is required to extract the yield drift profile

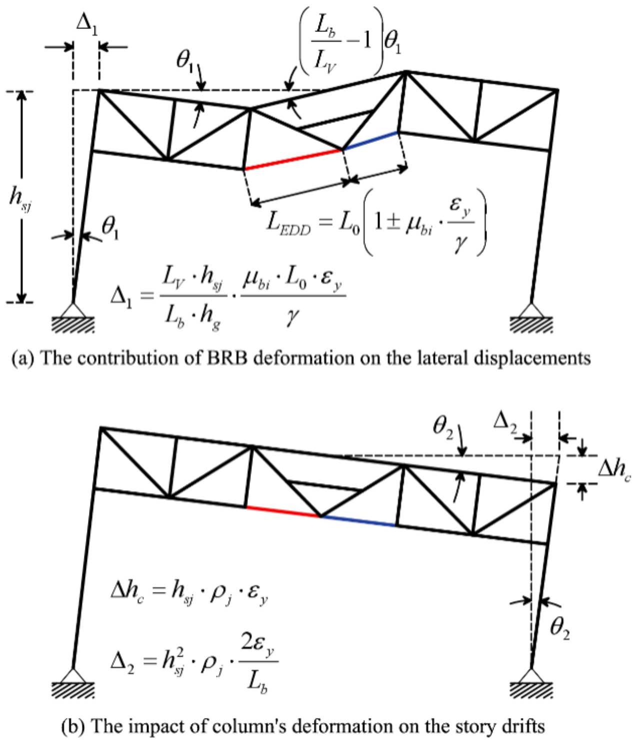

Fig. 7 The constituent components of lateral displacements

and also to characterize the substitute structure. In Eq. (6), the symbol μ_{bi} is the BRB's ductility ratio, ε_y is the structural steel's yield strain, ρ_j is the strain ratio between columns and the buckling-restrained braces ($\rho=\varepsilon_c/\varepsilon_b$) at the jth level, h_{sj} is the height of jth story and in accordance to Tsai *et al*. (2003), γ is a ratio to define the length of yielding core in BRBs.

3.2 Yield drift profile

The lateral yield displacement participates in the estimation of story ductilities and then to calculate the overall ductility of the system. By noticing that Eq. (6) is based on the strain ratios to define the drift profile, it is valid in the both elastic and inelastic conditions (Della Corte 2006). Accordingly, the yield drift profile can be inferred from Eq. (6) by taking the BRB ductility ratios in all levels as unity. Moreover, in order to simplify the procedure, various values of ρ_j in the Eq. (6) are replaced by an individual value of ρ in the Eq. (7). It means that the strain ratios at all levels are supposed to be identical.

$$\theta_{yi}=\frac{L_V\cdot L_0}{L_b\cdot h_g}\cdot\frac{\varepsilon_y}{\gamma}+\frac{2\varepsilon_y\cdot\rho\cdot h_i}{L_b} \tag{7}$$

in which h_i is the height of ith level from the base and the rest of parameters were defined earlier.

3.3 Substitute SDOF structure

The substitute SDOF is able to consider the overall condition of the HPR-TGF and acquire its seismic demands from a spectral displacement diagram. In this regard the lateral displacement properties of the system should be regarded properly. The major advantage of Eq. (6) is that the ductility ratio of BRBs is explicitly included in the specification of the drift profile. Thus, by applying a height wise distribution of BRB ductilities, it becomes possible to build up a linear profile for the ultimate lateral displacements. Such profile will minimize the base shear and enhance the energy dissipation capacity. In this regard, the entire phrase of Eq. (6) is replaced by a particular parameter of θ_c. This implies that the HPR-TGF will ultimately reach a linear displaced shape with the inclination of θ_c which is its target drift capacity. With this assumption, the design displacement, the effective mass and the effective height are as given by Eqs. (8), (9) and (10), respectively.

$$\Delta_d=\frac{\sum_{i=1}^{i=n}m_i\cdot h_i^2}{\sum_{i=1}^{i=n}m_i\cdot h_i}\cdot\theta_c \tag{8}$$

$$m_e=\frac{\left(\sum_{i=1}^{i=n}m_i\cdot h_i\right)^2}{\sum_{i=1}^{i=n}m_i\cdot h_i^2} \tag{9}$$

$$H_e=\frac{\sum_{i=1}^{i=n}m_i\cdot h_i^2}{\sum_{i=1}^{i=n}m_i\cdot h_i} \tag{10}$$

where m_i is the seismic mass lumped at the ith level.

3.4 Distribution of lateral forces

The theory of controlling failure mechanism proposed by Della Corte (2006) has some weaknesses beside its remarkable privileges. One of these deficiencies is that the drift profile merely depends on the first mode of vibrations. The same limitation has been declared by Maley *et al*. (2010) for the design of taller dual systems. In order to overcome such matters, an appropriate distribution of lateral forces which accounts for the higher mode effects should be applied in the design process. According to a comparison made by Mohammadi and Sharghi (2014) among various shear distributions, it's been deduced that the inelastic pattern of lateral forces proposed by Chao *et al*. (2007) generates more uniform story deformations along the height of structure. The aforementioned distribution of lateral forces is given through Eqs. (11) to (13). It should be noted that the effective period of vibrations (T_e) has been embedded in these equations to make them compatible with the direct displacement based design procedure. Moreover, the estimation of λ factor which is the distribution exponent requires a series of nonlinear dynamic analysis.

$$F_i=(\beta_i-\beta_{i+1})F_n \quad \text{when} \quad i=n \quad \text{then} \quad \beta_{n+1}=0 \tag{11}$$

$$F_n=V_d\left(\frac{w_n h_n}{\sum_{j=1}^{j=n}w_j h_j}\right)^{\lambda T_e^{-0.2}} \tag{12}$$

$$\beta_i=\frac{V_i}{V_n}=\left(\frac{\sum_{j=i}^{j=n}w_j h_j}{w_n h_n}\right)^{\lambda T_e^{-0.2}} \tag{13}$$

the symbols F_i and F_n are lateral forces exerting at the ith and roof (nth) levels, respectively. β_i is the shear distribution factor and it plays a significant role in the capacity distribution of energy dissipating devices. V_d is the design base shear and V_i is the story shear at the ith level. $w_j h_j$ and $w_n h_n$ are respectively the product of seismic weights lumped at the jth and nth (roof) stories multiplied by the story heights at the considered levels.

3.5 Overall ductility demand

Since various components of the HPR-TGF such as columns and energy dissipating devices are participating in its lateral sway mechanism, different ductility layouts can be specified. The major representations of these layouts are the story ductility and the BRB ductility. The story ductility is depending on the entire deformation characteristics of the story which defines the ratio between target drift capacity and the yield drift at each level ($\mu_i = \theta_c/\theta_{yi}$). The BRB ductility is for the design of BRBs and will be explained in the forthcoming sections. However, the overall ductility of the system must encompass all of these characteristics. Accordingly, multiple story ductilities along the height of HPR-TGF has been weighted in proportion to their energy dissipation capacities. Thus, Eq. (14) is presented to express the overall ductility of the system.

$$\mu_{sys} = \frac{\sum_{i=1}^{i=n} \mu_i \cdot V_i \cdot \theta_c}{\sum_{i=1}^{i=n} V_i \cdot \theta_c} = \frac{\sum_{i=1}^{i=n} \mu_i \cdot \beta_i}{\sum_{i=1}^{i=n} \beta_i} \qquad (14)$$

3.6 Equivalent damping

The Overall damping of HPR-TGFs, as expressed by Eq. (15), is consisting of inherent, viscous and hysteretic damping. Generic mathematical models for the determination of energy dissipation in structures do not capture some factors such as the elastic nonlinearity (response is not perfectly linear in the elastic range), damping associated with foundation compliance, foundation nonlinearity and additional damping due to the interaction of structural and nonstructural elements. Thus, the inherent damping will account for all of these mechanisms which have not been explicitly involved in the structural analysis. Accordingly, the common value of $\xi_i = 2\%$ is chosen as the inherent damping of the HPR-TGF systems. Moreover, the proposed HPR-TGF configuration is potentially capable of providing some extra rate-dependent energy dissipation through the functioning of Fluid Viscous Dampers (FVDs). The value of ξ_{vsc} is the damping ratio of FVDs and it will be used subsequently for the design of dampers.

$$\xi_{eq} = \xi_i + \xi_{vsc} + \xi_{hst} \qquad (15)$$

3.6.1 Hysteretic damping

The above mentioned definition of viscous damping helps to simplify the solution of the differential equation of vibrations. Thus, an analogous approach will be undertaken for BRBs in terms of replacing their hysteretic behavior by an equivalent amount of viscous damping. This replacement provides a perfectly linear SDOF which is appropriate for the direct displacement based design process. However, the entire nonlinear characteristics of BRBs along the height of HPR-TGF will be summarized in the equivalent hysteretic damping coefficient (ξ_{hst}). The estimation of inelastic behavior through a parameter which is proportional to the velocity was initially proposed by Jacobsen (1930). The basic assumption in this early study is that the system subjects to harmonic excitations developing complete and closed-form hysteresis loops. Nevertheless, it is apparent that an actual earthquake does not produce an exact steady-state harmonic response and thus unknown errors may be included. Accordingly, Blandon and Priestley (2005) have proposed a new generation of equivalent viscous damping relations calibrated for different hysteretic rules using inelastic time-history analysis. In the present study, an overall bilinear response specified by the system's ductility ratio (μ_{sys}) is considered for the HPR-TGF. Thus, the equation of equivalent viscous damping for bilinear hysteretic response by Blandon and Priestley (2005), as expressed by Eq. (16), is regarded to define the hysteretic damping ratio of the system.

$$\xi_{hst} = \frac{123}{\pi}\left(1 - \frac{1}{\sqrt{\mu_{sys}}} - \frac{\eta \cdot \mu_{sys}}{10}\right)\left(1 + \frac{1}{(T_e + 0.85)^4}\right) \qquad (16)$$

in which T_e is the effective period of vibrations and η is the post-yield stiffness ratio for the bilinear response of the system.

3.7 Estimation of FVD capacities

A fluid viscous damper consists of a housing filled with a compound of silicone or a similar type of fluid which accommodates a piston head with orifices (Lee and Taylor 2001). The fluid flowing through orifices develops a desirable out-of-phase energy dissipation in the structure. The phase difference, as depicted in the Fig. 8(a), means that the maximum damping force (F_d) does not occur at the maximum displacement. Thus, Eq. (17) describes the velocity-dependent output force of FVDs.

$$F_d = C \cdot |v|^\alpha \cdot \mathrm{sgn}(v) \qquad (17)$$

where F_d is the damper force, v is the velocity, C is a constant expressed in units of force divided by velocity, α is an exponent specifying the characteristics of force-velocity relation and sgn is the signum function defining the sign of velocity. For typical seismic applications, α is less than or equal to one. As plotted in the Fig. 8(b), when α exactly equals to one, the damping force is proportional to the relative velocity in dampers and the device is called linear fluid viscous damper. In the case of $\alpha < 1$, dampers can develop larger resistive damping forces at small or intermediate velocities. Thus the design and utilization of nonlinear viscous dampers would be more economical than linear viscous dampers. The surface of surrounded area by the force-deformation plot in the Fig. 8(a) expressed by Eq. (18) represents the capacity of viscous energy dissipation in the system. Since the ultimate response of HPR-TGFs is in the inelastic range, the estimation of E_{vsc} is based on the effective period of vibrations.

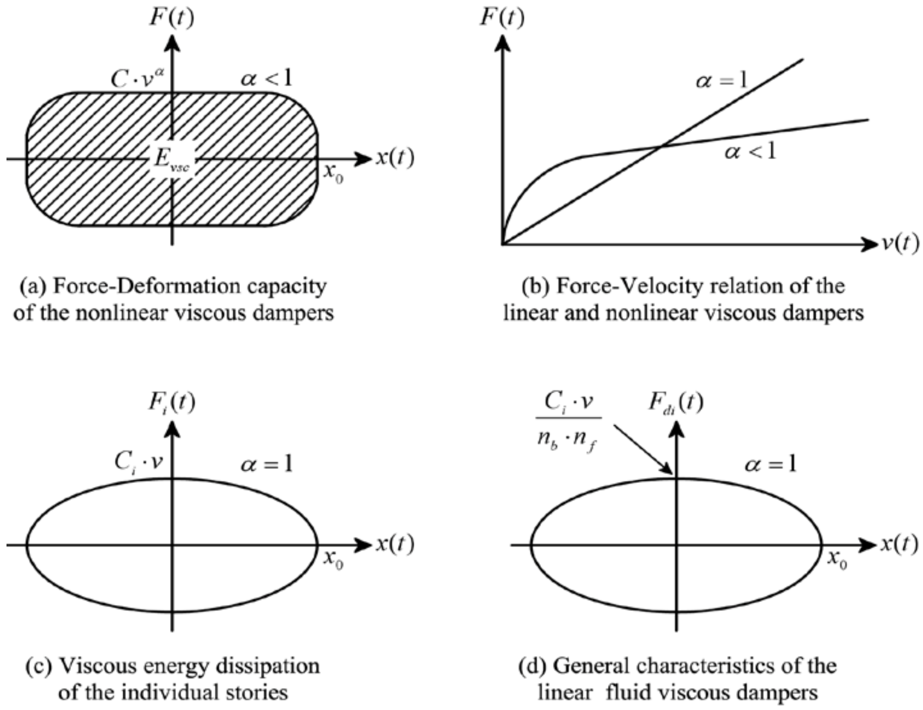

(a) Force-Deformation capacity of the nonlinear viscous dampers

(b) Force-Velocity relation of the linear and nonlinear viscous dampers

(c) Viscous energy dissipation of the individual stories

(d) General characteristics of the linear fluid viscous dampers

Fig. 8 Mechanical specifications of the viscous dampers

$$E_{vsc} = \oint F_d dx = \int_0^{T_e} F_d \cdot v dt \tag{18}$$

The value of F_d substitutes from Eq. (17) in the Eq. (18). The solution of the above mentioned expression is given by Eq. (19) in which Γ is the gamma function.

$$\begin{aligned} E_{vsc} &= 2^{(2+\alpha)} \cdot C \cdot x_0^{(1+\alpha)} \left(\frac{2\pi}{T_e}\right)^{\alpha} \times \frac{\Gamma^2\left(1+\left(\frac{\alpha}{2}\right)\right)}{\Gamma(2+\alpha)} \\ &= \lambda \cdot C \times x_0^{(1+\alpha)} \left(\frac{2\pi}{T_e}\right)^{\alpha} \end{aligned} \tag{19}$$

for linear viscous dampers ($\alpha = 1$), as depicted in the Fig. 8(c), the value of $\lambda = \pi$ will be resulted. It should be noted that x_0 is the deformation amplitude of FVDs and is given by considering θ_c in the Eq. (1). Accordingly, by applying the same pattern as the distribution of lateral forces for the vertical variation of damper capacities ($C_i = \beta_i \cdot C_n$), the viscous energy dissipation of the system can be rewritten as Eq. (20) for linear fluid viscous dampers.

$$\begin{aligned} E_{vsc} &= \sum_{i=1}^{i=n} \pi C_i \cdot x_0^2 \left(\frac{2\pi}{T_e}\right) \\ &= \pi C_n \left(\frac{L_b \cdot h_g}{L_V} \cdot \theta_c\right)^2 \left(\frac{2\pi}{T_e}\right) \sum_{i=1}^{i=n} \beta_i \end{aligned} \tag{20}$$

On the other hand, the capacity of viscous energy dissipation is aimed to damp the kinetic energy of the system. The overall kinetic energy of HPR-TGFs expressed by Eq. (21) is the summation of kinetic energies at the individual stories.

$$E_k = \sum_{i=1}^{i=n} \frac{m_i \cdot v_i^2}{2} = \frac{\theta_c^2}{2} \left(\frac{2\pi}{T_e}\right)^2 \cdot \sum_{i=1}^{i=n} m_i \cdot h_i^2 \tag{21}$$

In accordance to the principles of designing passive energy dissipation for structures by Constantinou *et al*. (1998), Eq. (22) is presented to relate the cyclic energy dissipation capacity of dampers and the kinetic energy of the structure.

$$\xi_{vsc} = \frac{E_{vsc}}{4\pi E_k} \tag{22}$$

by substituting the corresponding values of E_{vsc} and E_k from the Eqs. (20) and (21), the overall damping capacity requiring for the roof (nth) level declares by Eq. (23).

$$C_n = \frac{4\pi \cdot \xi_{vsc} \cdot L_V^2 \cdot \sum_{i=1}^{i=n} m_i h_i^2}{T_e \cdot L_b^2 \cdot h_g^2 \cdot \sum_{i=1}^{i=n} \beta_i} \tag{23}$$

The capacity of jth damper at the ith level, as expressed by Eq. (24) and shown in the Fig. 8(d), is depending on the number of frames (n_f) and the number of bays (n_b) in each direction.

$$C_i^j = \frac{\beta_i \cdot C_n}{n_b \cdot n_f} \tag{24}$$

Eventually, the pseudo velocity demands have been applied in the Eq. (25) to estimate the peak force of dampers.

$$F_{di}^j = \frac{2\pi \cdot L_b \cdot h_g}{T_e \cdot L_V} \cdot C_i^j \cdot \theta_c \tag{25}$$

in which F_{di}^j is the force developed in the jth damper at the ith level.

3.8 Vertical distribution of BRB strengths

The design continues by the estimation of arrival hysteretic energy at the system which is the starting step to define the strength of BRBs for HPR-TGF systems. In accordance to the basics of the DDBD procedure, the effective stiffness of the equivalent substitute structure (Eq. (4)) has been applied to characterize the amount of energy flow in the system. Thus, it can be concluded that the current definition of the system's input energy (hatched area in the Fig. 9(a)) is the hysteretic energy and will be dissipated through the functioning of BRBs.

The surface of hatched areas in the Fig. 9(a) and (b) are identical. Accordingly, with reference to the Fig. 9(b) the input energy of the system is as the following

$$\begin{aligned} E_{sys} &= (K_{sys} \cdot \Delta_y) \\ &\times \left(\Delta_d - \frac{K_{sys} \cdot \Delta_y + \eta K_{sys}(\Delta_d - \Delta_y)}{K_{sys}}\right) \\ &= K_{sys} \cdot \Delta_y^2 (\mu_{sys} - 1)(1 - \eta) \end{aligned} \tag{26}$$

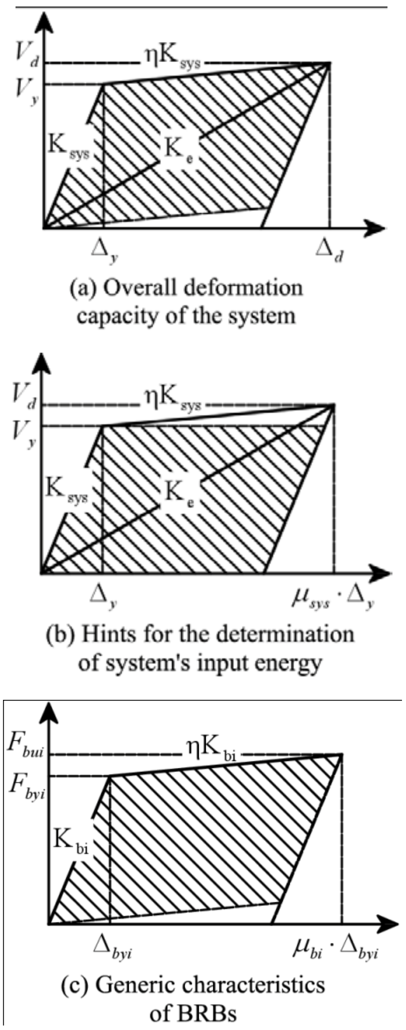

Fig. 9 Description of the system's input energy and its dissipation mechanism

Based on the geometric proportions in the Fig. 9(a) the system's initial stiffness (K_{sys}) can be rewritten as a function of its effective stiffness

$$K_{sys} = \frac{K_e \cdot \mu_{sys}}{1 + \eta(\mu_{sys} - 1)} \tag{27}$$

With the assumption of $\Delta_d = \mu_{sys} \cdot \Delta_y$, Eq. (28) will be declared as the input energy of the system.

$$\begin{aligned} E_{sys} &= K_e \cdot \Delta_d^2 \\ &\times \frac{(\mu_{sys} - 1)(1 - \eta)}{\mu_{sys}\left(1 + \eta(\mu_{sys} - 1)\right)} \end{aligned} \tag{28}$$

Afterward, by assuming that the distribution of BRB strengths along the height of HPR-TGF is proportional to the story shears at each level ($K_{bi} = \beta_i \cdot K_{bn}$), the ratio between energy dissipation capacities of the BRBs at the ith and the nth (roof) stories is as the following

$$\frac{E_{bi}}{E_{bn}} = \frac{K_{bi}(\mu_{bi} - 1)(1 - \eta)}{K_{bn}(\mu_{bn} - 1)(1 - \eta)} = \beta_i \cdot \frac{\mu_{bi} - 1}{\mu_{bn} - 1} \tag{29}$$

The accumulation of energy dissipation capacities along the height of HPR-TGF represents the entire amount of arrival hysteretic energy to the system (E_{sys}). Thus, Eq. (30) can be written as a function of the system's input energy.

$$E_{bn} = \frac{E_{sys}(\mu_{bn} - 1)}{\sum_{i=1}^{i=n} \beta_i (\mu_{bi} - 1)} \tag{30}$$

With reference to the Fig. 9(c), the initial stiffness of jth BRB at the ith level (K_{bi}^j) is given by Eq. (31) in which n_f is the number of frames in each direction and n_b is the number of bays in each frame.

$$K_{bi}^j = \frac{E_{bi}}{n_b \cdot n_f} \times \left[L_0^2 \left(\frac{\varepsilon_y}{\gamma}\right)^2 (\mu_{bi} - 1)(1 - \eta)\right]^{-1} \tag{31}$$

The symbol μ_{bi} is the BRB ductility at the ith level expressed by Eq. (32) in which θ_{yi} is defined by Eq. (7). The θ_{byi} is lateral drifts at the yielding instance of BRBs. The value of θ_{byi} can be inferred by getting $\rho = 0$ in the Eq. (7).

$$\mu_{bi} = \frac{\theta_c - \theta_{yi}}{\theta_{byi}} \tag{32}$$

The ultimate force developing in BRBs is due to the initial stiffness and the post-yield stiffness. Therefore, Eq. (33) is provided to estimate the required design forces in association with each BRB.

$$F_{bui}^j = K_{bi}^j \cdot L_0 \cdot \frac{\varepsilon_y}{\gamma}(1 + \eta(\mu_{bi} - 1)) \tag{33}$$

This equation will be utilized subsequently for the design of other elements.

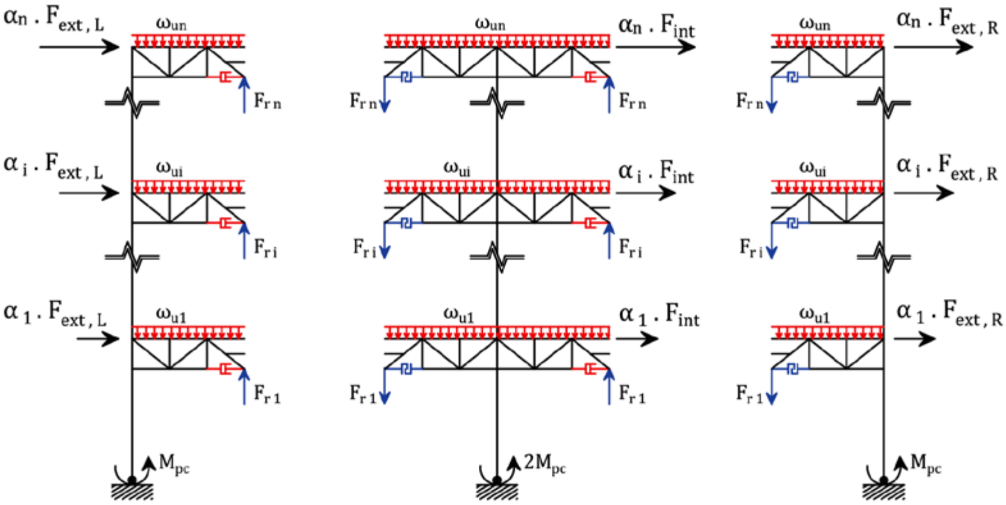

Fig. 10 Free body diagrams for the internal and external columns

3.9 Design of structural components

The design objective for structural members is to retain their elastic performance up to the ultimate displacement demands. Thus, by assuming that the bay lengths on the either side of interior columns are identical, Eqs. (34) and (35) have been derived based on the free body diagrams in the Fig. 10.

$$F_{int} = \frac{1}{\sum_{i=1}^{i=n} \alpha_i h_i} \left(L_b \sum_{i=1}^{i=n} F_{ri} + 2M_{pc} \right) \tag{34}$$

$$F_{extR,L} = \frac{1}{\sum_{i=1}^{i=n} \alpha_i h_i} \times \left(\frac{L_b}{2} \sum_{i=1}^{i=n} F_{ri} \pm \frac{L_b^2}{8} \sum_{i=1}^{i=n} \omega_{ui} + M_{pc} \right) \tag{35}$$

where F_{int}, $F_{ext,R}$ and $F_{ext,L}$ are the sum of lateral forces acting on internal columns, right side external columns and the left side external columns, respectively. α_i is the lateral load distribution ratio given by Eq. (36), M_{pc} as defined by Leelataviwat *et al*. (1999) through Eq. (37) is an initial estimation for the plastic moments at the first story columns and F_{ri} is the ultimate resistive shear forces developing on the detachment axis of the Fig. 10 diagrams which is given by Eq. (38).

$$\alpha_i = \frac{F_i}{\sum_{i=1}^{i=n} F_i} = \frac{(\beta_i - \beta_{i+1})}{\sum_{i=1}^{i=n} (\beta_i - \beta_{i+1})} \tag{36}$$

$$M_{pc} = \frac{1.1V' \cdot h_1}{4} \tag{37}$$

$$F_{ri} = \frac{h_g}{L_V} (F_{di} + F_{bui}) \tag{38}$$

In the Eq. (37), V' is the shear force in a single bay at the base level and h_1 is the height of first story. The symbols F_{di} and F_{bui} which are involved in the Eq. (38) will be defined with reference to the Eqs. (25) and (33), respectively.

4. Verification of the design procedure

The case study structure is a nine-story building with 45.72 m × 45.72 m in plan and 39.62 m in elevation where is located at San Francisco. The perimeter HPR-TGFs as depicted in the Fig. 11(a) will form the lateral load bearing system for this building. Its target drift capacity is chosen to be $\theta_c = 1.5\%$ for the maximum credible earthquake (2% in 50 years hazard level). Hence, the site specifications in accordance to the ASCE7 (2010) provisions are $S_{MS} = 1.50$ g and $S_{M1} = 0.78$ g. Horizontal displacements at the ground level are restrained by concrete foundation walls and the surrounding soils. Interior simple frames are accompanied by composite floors to form the gravitational load bearing system. The perimeter HPR-TGFs are designed to withstand a series of concentrated point loads with the magnitude of 71.17 kN at the regular intervals of 3.05 m on the top chords of trusses. Columns are wide-flange 345 MPa steel sections. The value of $\xi_{vsc} = 15\%$ is considered as the additional amount of viscous damping due to the functioning of FVDs. It's also assumed that the pure yielding extent of BRBs is up to 87% of their lengths ($\gamma = 1.15$). Moreover, with reference to the Fig. 11(b), the HPR-TGF and its design process have been evaluated through a benchmark BRB-STMF previously proposed by Pekcan *et al*. (2009) as the seismic load bearing system for the same building. The seismic masses and characteristics of the substitute SDOF structure listed in the Table 1 are associated with two HPR-TGFs in each direction. Probable seismic excitations are simulated via nine amplitude scaled time-history records from the PEER (2016) database presented in the Table 2. The spectral acceleration of these records in comparison to the ASCE7 (2010) target spectrum has been plotted in the Fig. 12(a). The scaling process is done using instructions outlined in ASCE7 (2010) Section 16.1.3.1 within the period range of $0.2T$ to $1.5T$ in

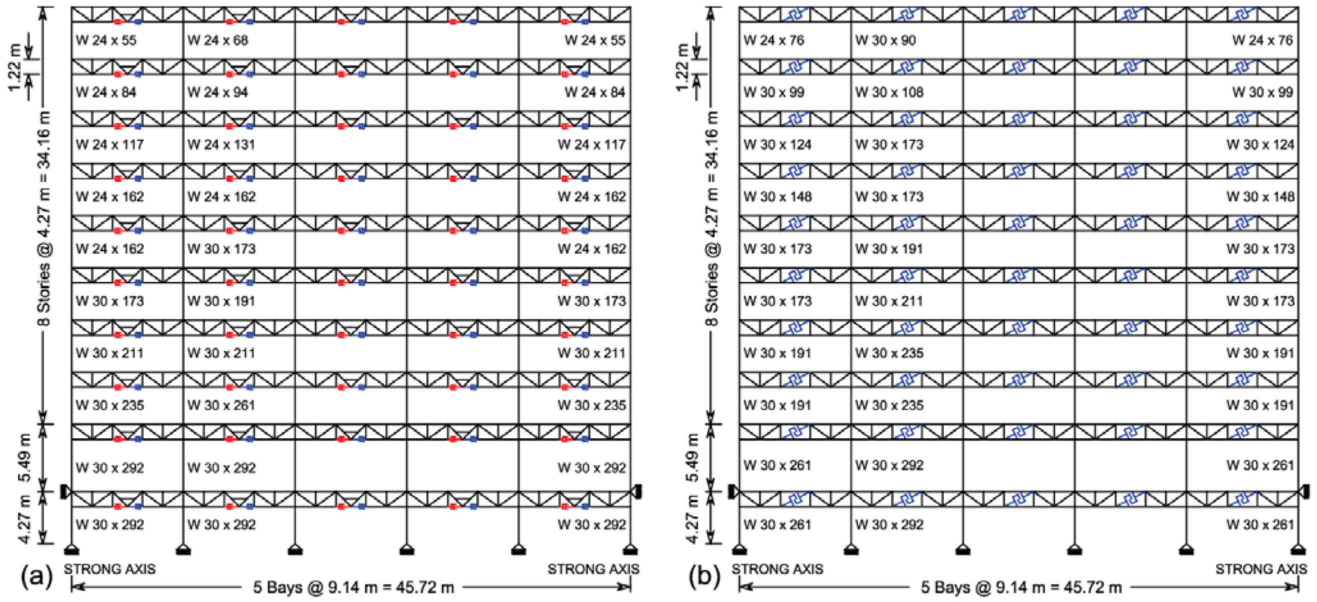

Fig. 11 Structural configuration and cross sections in (a) HPR-TGF; and (b) the benchmark BRB-STMF systems

Table 1 Detailed calculations for the substitute SDOF

Level	h_i (m)	m_i (tons)	m_ih_i	m_ih^2	Δ_d (m)	m_e (tons)	h_e (m)
9	39.62	1069.12	42363	1678578	0.422	7258.55	28.11
8	35.36	988.83	34962	1236140			
7	31.09	988.83	30742	955767			
6	26.82	988.83	26523	711405			
5	22.56	988.83	22303	503055			
4	18.29	988.83	18084	330715			
3	14.02	988.83	13864	194387			
2	9.75	988.83	9645	94070			
1	5.49	1007.88	5530	30338			
G.L.	0	963	0	0			
			204015	5734456			

which T is the fundamental period of the case study structure. After completing the iteration loop in the Fig. 6 with the aid of an appropriately damped displacement spectra (Fig. 12(b)), the values of $\xi_{eq} = 39.1\%$ and $T_e = 4.498$ s will be declared as the equivalent damping capacity and the effective period of vibrations, respectively. In accordance to Priestley *et al*. (2007) the amplitude scaling of earthquake records is possibly forming a large scatter in the displacement spectrum. However, the average of spectral displacements (bold dashed line in the Fig. 12(b)) must match the design displacement spectrum within the range of the period shift in which the inelastic response of HPR-TGF is expected. In the case of current study with the fundamental period of T = 2.126 s a perfect match between the average of spectral displacements and the target displacement spectrum is observed and also a margin of about T = 1.0 s exists for the period shift which is considered to be adequate.

Table 2 Ground motion records for the nonlinear time history analysis

Label	RSN	Year	Event	Mag	Scale factor	PGA(g)
EQ-1	6	1940	Imperial Valley, Array #9	6.95	1.9	0.853
EQ-2	180	1979	Imperial Valley, Array #5	6.53	1.6	0.952
EQ-3	514	1986	North Palm Springs	6.06	2.9	0.641
EQ-4	767	1989	Loma Prieta, Gilroy	6.93	3.9	2.180
EQ-5	838	1992	Landers, Bastrow	7.28	3.2	0.473
EQ-6	900	1992	Landers, Yermo	7.28	2.0	0.593
EQ-7	1044	1994	Northridge, Newhall	6.69	2.1	1.691
EQ-8	1084	1994	Northridge, Sylmar	6.69	1.0	0.748
EQ-9	1085	1994	Northridge, Sylmar	6.69	1.4	0.629

4.1 Inelastic design parameters

One of the major challenges in the seismic design of HPR-TGFs using the DDBD procedure is the adjustment of their ultimate performance in accordance to actual nonlinear time-history analysis. An analogous issue for the direct displacement based design of single column bridge piers has been investigated by Tecchio *et al*. (2015) in terms of providing accuracy estimation for various design conditions. In the case of HPR-TGFs, the presence of parameters such as ρ in the Eq. (7) and λ in the Eqs. (12)

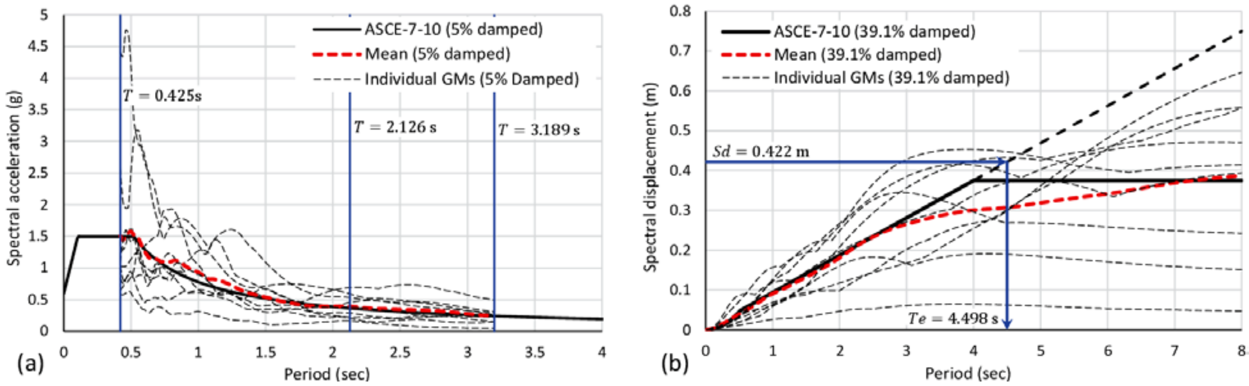

Fig. 12 Spectral representation of (a) acceleration; and (b)displacement responses

Table 3 The impact of inelastic design parameters on the design outcomes

Level	Interior columns	Exterior columns	K_{bi} (kN/mm)	C_i (N.s/mm)	Interior columns	Exterior columns	K_{bi} (kN/mm)	C_i (N.s/mm)	Interior columns	Exterior columns	K_{bi} (kN/mm)	C_i (N.s/mm)
λ = 1.0	ρ = 0.0				ρ = 0.5				ρ = 1.0			
9th	W14X82	W14X68	31.0	509.4	W14X132	W24X68	90.9	537.1	W14X132	W14X68	139.4	573.6
8th	W24X84	W24X76	48.3	792.6	W14X159	W14X132	142.3	840.7	W14X283	W14X120	219.7	904.9
7th	W24X103	W24X94	61.7	1013.0	W14X193	W14X159	182.5	1078.6	W14X398	W14X193	282.9	1166.2
6th	W18X130	W24X104	72.5	1191.0	W14X211	W14X176	214.8	1269.8	W24X335	W14X233	334.0	1376.4
5th	W24X117	W24X117	81.1	1332.6	W14X233	W14X211	240.8	1423.1	W24X370	W14X257	375.1	1544.2
4th	W24X131	W24X131	87.9	1443.5	W14X283	W14X257	261.1	1542.8	W24X370	W24X207	407.3	1677.1
3rd	W24X131	W24X146	93.0	1526.7	W14X342	W14X283	276.4	1633.3	W24X306	W24X207	431.5	1777.8
2nd	W18X158	W24X146	96.4	1583.7	W14X398	W14X342	286.8	1694.6	W30X326	W24X250	448.0	1844.9
1st	W24X176	W24X162	98.4	1615.8	W14X500	W14X398	292.7	1729.6	W30X357	W30X326	457.4	1884.3
Overall	7.38 tons	6.92 tons	T = 2.683 s		16.47 tons	13.59 tons	T = 2.315 s		18.91 tons	12.41 tons	T = 1.955 s	
λ = 1.5	ρ = 0.0				ρ = 0.5				ρ = 1.0			
9th	W14X53	W16X50	19.4	318.2	W14X82	W14X68	54.8	331.3	W14X82	W14X53	81.0	350.3
8th	W14X99	W14X99	37.6	617.4	W14X132	W14X120	107.2	649.5	W14X211	W14X74	160.1	693.3
7th	W14X132	W14X132	54.3	891.8	W14X176	W14X159	155.6	942.9	W14X311	W14X132	233.9	1013.0
6th	W14X159	W14X159	69.1	1135.6	W14X211	W14X193	198.7	1204.2	W24X279	W14X176	299.9	1297.6
5th	W24X131	W14X176	81.9	1344.3	W14X257	W14X233	235.8	1427.5	W24X335	W14X211	356.7	1544.2
4th	W24X146	W14X193	92.3	1516.5	W14X311	W14X257	266.2	1612.8	W24X335	W24X176	403.6	1747.1
3rd	W24X162	W14X211	100.4	1647.9	W14X370	W14X311	289.9	1755.9	W24X279	W24X192	440.0	1903.3
2nd	W24X162	W14X211	106.0	1741.3	W14X426	W14X342	306.4	1855.1	W30X326	W24X279	465.5	2014.2
1st	W24X176	W14X233	109.3	1795.3	W30X326	W14X398	315.9	1913.5	W30X391	W30X357	480.2	2078.5
Overall	8.07 tons	9.72 tons	T = 2.701 s		15.14 tons	13.93 tons	T = 2.259 s		16.89 tons	11.12 tons	T = 1.993 s	
λ = 2.0	ρ = 0.0				ρ = 0.5				ρ = 1.0			
9th	W14X38	W14X48	11.9	195.6	W14X53	W14X61	32.7	201.4	W14X53	W14X48	46.9	211.6
8th	W14X74	W14X90	28.8	472.9	W14X109	W14X109	79.8	493.3	W14X145	W14X74	116.2	522.5
7th	W14X120	W14X132	47.0	772.1	W14X159	W14X159	131.2	811.5	W14X257	W14X99	192.5	867.0
6th	W14X159	W14X159	64.9	1065.5	W14X211	W14X193	181.7	1123.9	W24X229	W14X132	267.9	1205.6
5th	W24X131	W14X193	81.3	1335.5	W14X283	W14X233	228.2	1411.4	W24X279	W14X176	337.5	1519.4
4th	W24X146	W14X211	95.4	1566.1	W14X342	W14X283	268.3	1658.1	W24X306	W24X162	397.8	1790.9
3rd	W24X162	W14X233	106.7	1751.5	W14X398	W14X311	300.5	1858.1	W24X279	W24X207	446.3	2009.9
2nd	W24X176	W14X233	114.8	1885.8	W30X292	W14X370	323.5	1999.6	W30X326	W30X261	481.1	2166.0
1st	W24X192	W14X233	119.5	1963.2	W30X357	W14X426	337.0	2082.8	W33X387	W30X357	501.4	2258.0
Overall	7.95 tons	10.15 tons	T = 2.702 s		14.64 tons	14.39 tons	T = 2.238 s		15.06 tons	10.27 tons	T = 2.046 s	

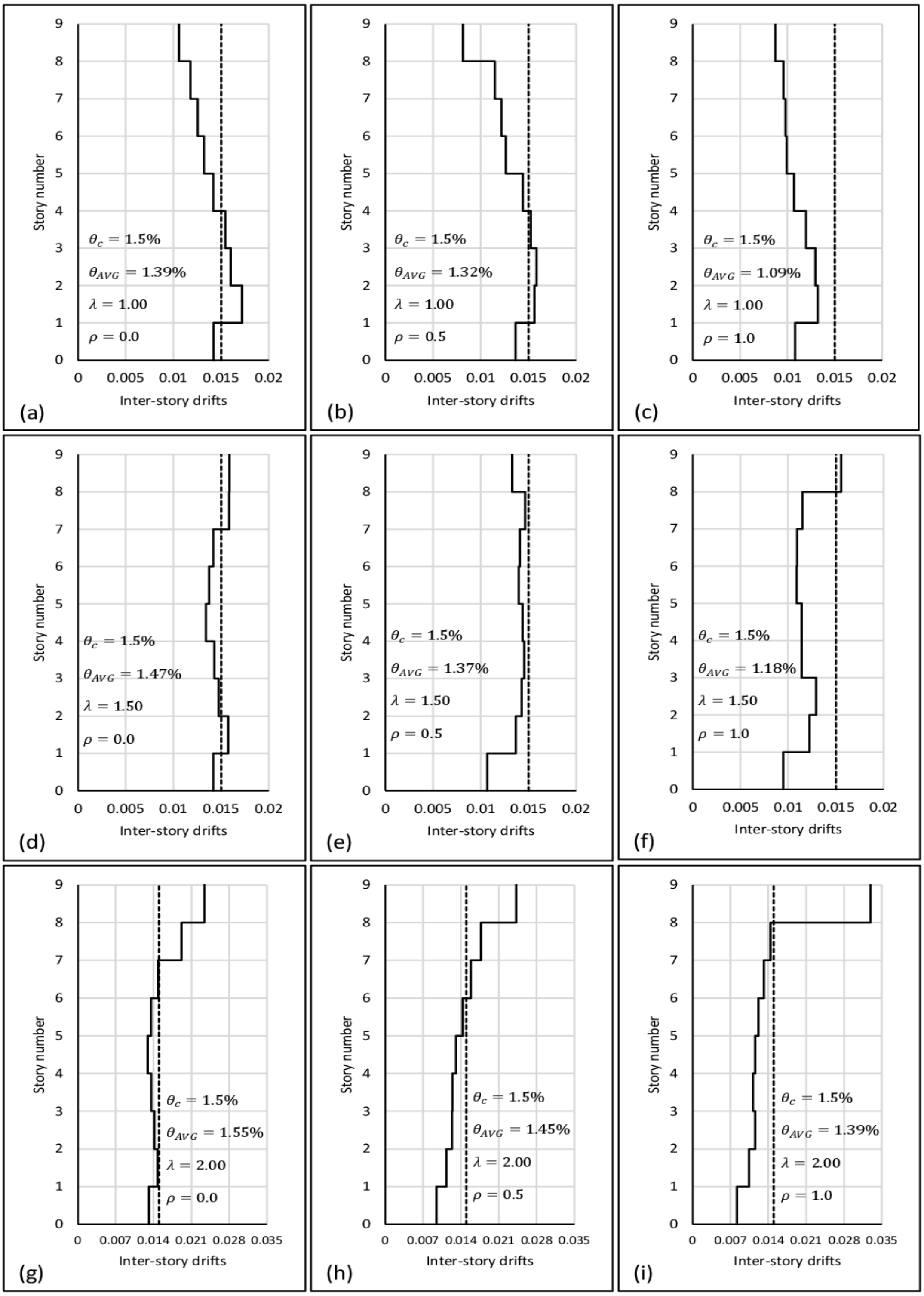

Fig. 13 Effects of inelastic design parameters on the overall inter-story drifts

and (13) is for adjusting the ultimate behavior of HPR-TGF systems. Among these parameters the estimation of optimum value for the λ factor as expressed by Chao *et al*. (2007), requires a series of design and analysis of the structure. This process has been done for the case study HPR-TGF and the results are presented in the Table 3 as well as Figs. 13 and 14. According to the overall column weights in the Table 3, it is evident that by applying non-zero ρ factors the consumption of structural steel will be increased. However, this is necessary to enhance the robustness of the frame and thus the fundamental period of vibrations decreases. Further investigations regarding the structural variations in the Table 3 have been presented in the Fig. 13 using SAP2000 (2015) as an integrated finite element analysis and design software to conduct the nonlinear time-history analysis. The analytical models are in 2D condition and dummy column is embedded in the model to include the added moment due to the gravitational loads of interior frames. FVDs and BRBs are modeled using nonlinear Damper-Exponential and Plastic (Wen) type nonlinear link elements. In accordance to the Fig. 13, if the λ factor is less than its optimum value the design outcomes in the higher stories will become overestimated (Figs. 13(a), (b) and (c)). On the other hand, when λ is more than its optimum value, design strengths will be underestimated leading to the detrimental effects due to higher modes (Figs. 13(g), (h) and (i)). Since none of the above-mentioned circumstances is capable of forming a practically linear displacement profile, the optimum value of λ must be chosen wisely to achieve the design goals (Figs. 13(d), (e) and (f)). Another typical pattern which can be deduced from the Fig. 13 is that by applying higher ρ values at a constant magnitude of λ, the average of practical inter-story drifts (θ_{AVG}) decreases. On the other hand, the concept of Deviation from Target drift Capacity (DTC) which is given by the following equation has been applied in the Fig. 14 to evaluate the accuracy of the design procedure.

$$DTC = \sqrt{(1/n)\sum_{i=1}^{i=n}(\theta_c - \theta_i)^2} \tag{39}$$

In accordance to the Fig. 14, as the λ factor reaches its optimum value the deviation from target drift capacity decreases and the design precision will be increased subsequently. The interaction of inelastic design parameters in the Fig. 14 indicates that the ρ factor has no impact on the optimum value of the λ factor, but the application of higher ρ values which improves the robustness of the frame, leads to increasing the value of DTC in a conservative manner. Despite certain values of these parameters are leading to very precise outcomes, but always there should be a margin of safety by enhancing the robustness of the frame. For example, designing the case study HPR-TGF for $\theta_c = 1.5\%$ with the assumption of $\lambda = 1.5$ and $\rho = 0.0$ is practically resulting in $\theta_{AVG} = 1.47\%$ which is considerably accurate ($DTC = 9.49 \times 10^{-4}$), but its lateral stiffness might be insufficient. Thus, non-zero ρ values may be applied to increase its lateral stiffness. In order to evaluate the performance of the proposed HPR-TGF configuration in comparison to the benchmark structure, the expedient values of $\rho = 0.4$ and $\lambda = 1.5$ are chosen to get similar results as the benchmark structure.

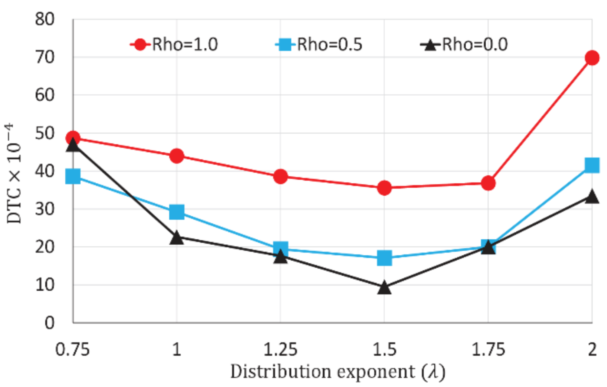

Fig. 14 Interaction of the inelastic design parameters

4.2 The base shear

By applying the basic equations of the Direct Displacement Based Design approach from Eqs. (4) and (5), the effective stiffness and the design base shear is given as the following

$$K_e = 4\pi^2 \cdot \frac{m_e}{T_e^2} = 4\pi^2 \cdot \frac{7258.55}{4.498^2} = 14163.5\ kN/m$$

$$V_d = K_e \cdot \Delta_d = 14163.5 \times 0.422 = 5977\ kN$$

4.3 Major requirements of the design

By considering Table 4 and assuming that the post yield stiffness ratio of the system specified by BRBs is $\eta = 5\%$, the basic energy dissipation properties of the system as defined by Eqs. (14), (28) and (30) are given in the following

$$\mu_{sys} = \frac{\sum_{i=1}^{i=n}\mu_i \cdot \beta_i}{\sum_{i=1}^{i=n}\beta_i} = \frac{213.72}{35.04} = 6.10$$

$$E_{sys} = K_e \cdot \Delta_d^2 \cdot \frac{(\mu_{sys}-1)(1-\eta)}{\mu_{sys}\left(1+\eta(\mu_{sys}-1)\right)}$$
$$= 14163.5 \times 0.422^2 \times \frac{(6.1-1)(1-0.05)}{6.1\left(1+0.05(6.1-1)\right)}$$
$$= 1596.3 kN.m$$

$$E_{bn} = E_{sys}(\mu_{bn}-1)\left[\sum_{i=1}^{i=n}\beta_i(\mu_{bi}-1)\right]^{-1}$$
$$= \frac{1596.3 \times (21.57-1)}{1004.23} = 32.7\ kN.m$$

4.4 Design of energy dissipating devices

The contribution of energy dissipation assigned to the BRBs at each level (E_{bi}) is expressed in the Table 5. This parameter is required to estimate the stiffness of BRBs (K_{bi}). Other characteristics of BRBs such as their yielding and ultimate forces (F_{byi} and F_{bui}) and also the damping capacity of FVDs (C_i) and the peak force exerted by FVDs (F_{di}) are given in the Table 5 as well. Values in this table are presented for one device while others in each level are identical.

4.5 Structural cross sections

The design forces required to estimate proper cross sections for the structural elements is presented in the Table 6. The corresponding values of lateral load distribution ratio (α_i) are also mentioned in this table. Thus the lateral forces acting on the internal columns (F_{int}), external columns ($F_{extR,L}$) and the ultimate resistive forces due to energy

Table 4 Details of the major parameters required for the design

Level	θ_{yi} (%)	β_i	μ_i	$\beta_i \cdot \mu_i$	μ_{bi}	$\beta_i\,(\mu_{bi}-1)$
9	0.638	1.00	2.35	2.35	21.57	20.57
8	0.573	1.95	2.62	5.10	23.18	43.27
7	0.509	2.83	2.95	8.34	24.79	67.30
6	0.445	3.61	3.37	12.18	26.40	91.69
5	0.380	4.28	3.95	16.88	28.01	115.60
4	0.316	4.83	4.75	22.94	29.62	138.27
3	0.251	5.26	5.96	31.36	31.23	158.95
2	0.187	5.56	8.02	44.55	32.84	176.94
1	0.123	5.73	12.22	70.01	34.45	191.64
Sum	-	35.04	-	213.72	-	1004.23

Table 5 Detailed characteristics of EDDs

Level	E_{bi} (kN.m)	K_{bi} (kN/mm)	F_{byi} (kN)	F_{bui} (kN)	C_i (N.s/mm)	F_{di} (kN)
9	32.7	50.0	91.3	185.3	327.9	31.4
8	68.8	97.5	178.2	375.8	639.6	61.3
7	107.0	141.4	258.4	565.7	927.5	88.9
6	145.8	180.4	329.7	748.4	1183.5	113.4
5	183.8	213.9	390.9	918.8	1403.2	134.4
4	219.8	241.4	441.3	1072.7	1583.9	151.8
3	252.7	262.7	480.2	1206.1	1723.9	165.2
2	281.3	277.7	507.6	1315.5	1821.9	174.6
1	304.6	286.3	523.3	1398.4	1878.4	180.0

Table 6 Summary of the design forces

Level	$\beta_i - \beta_{i+1}$	α_i	$F_{ext,L}$ (kN)	F_{int} (kN)	$F_{ext,R}$ (kN)	F_{ri} (kN)
9	1.00	0.175	123.8	271.1	147.3	108.3
8	0.95	0.166	117.7	257.8	140.1	218.5
7	0.88	0.153	108.7	238.1	129.4	327.3
6	0.78	0.136	96.6	211.7	115.0	430.9
5	0.67	0.117	82.9	181.7	98.7	526.6
4	0.55	0.096	68.2	149.4	81.2	612.2
3	0.43	0.075	52.8	115.7	62.9	685.6
2	0.30	0.052	37.0	81.1	44.1	745.1
1	0.17	0.030	21.3	46.7	25.4	789.2
Sum	5.73	-	-	-	-	-

dissipating devices (F_{ri}) along the height HPR-TGF are as given by Table 6. The steel sections assigned to columns are as depicted in the Fig. 11(a). The design outcomes for trusses are presented in the Fig. 15 as well as the Table 7. Double channel sections are considered for the design of truss components. In order to enhance the rigidity of trusses, the same sections is applied for the chord members in each truss. The adjacent chords to columns (C2 in the Fig. 15) are reinforced by welded plates over the whole length of the corresponding panel.

4.6 Pushover analysis results

A pushover comparison among the benchmark structure and some of the possible design conditions of HPR-TGF is presented in this section. Since the inter-story drifts in association with the target displacement are not significantly large, the P-Δ effects did not include in the analysis. In other words, the additional lateral strength of interior frames, as well as the P-Δ effects, have been ignored simultaneously. Moment-rotation characteristics of

Table 7 Structural details for the truss components

Floor	C2 (Plate thickness)	C1	VSL	D	V
9	6C8.2X(0.25”)	6C8.2	3C3.5	3C5	3C3.5
8	6C10.5X(0.5”)	6C10.5	4C5.4	5C9	3C3.5
7	7C12.25X(0.75”)	7C12.25	5C6.7	6C8.2	3C3.5
6	9C20X(0.75”)	9C20	6C8.2	6MC12	3C3.5
5	10C30X(1.00”)	10C30	6C10.5	6MC12	3C3.5
4	10C30X(1.00”)	10C30	7C9.8	6MC16.3	3C3.5
3	12C30X(1.25”)	12C30	7C12.25	6MC16.3	3C3.5
2	12C30X(1.25”)	12C30	7C12.25	6MC16.3	3C3.5
1	15C33.9X(1.25”)	15C33.9	7C14.75	6MC16.3	3C3.5
Ground	15C33.9X(1.25”)	15C33.9	7C14.75	6MC16.3	3C3.5

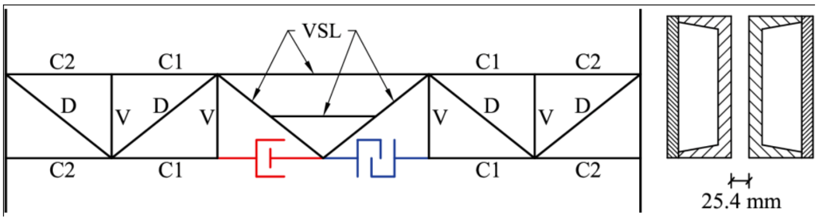

Fig. 15 Structural properties of the truss components

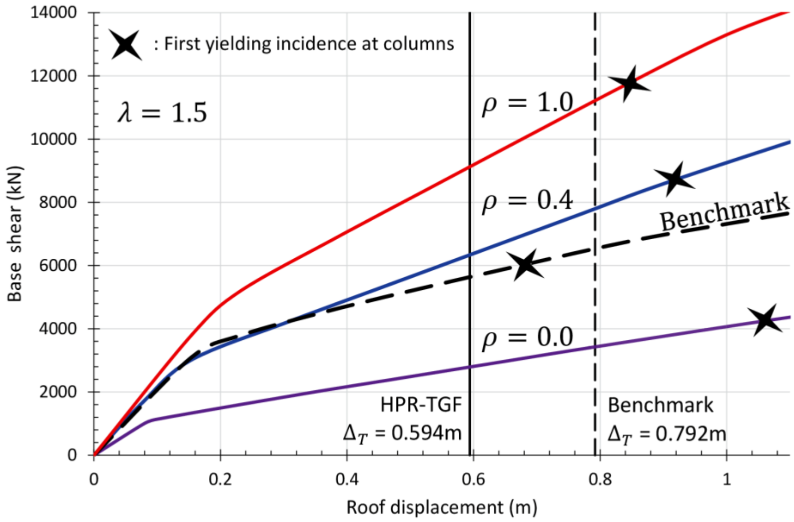

Fig. 16 Comparison of various pushover capacity curves

the plastic hinges have generally followed the ASCE41 (2006) recommendations. Nevertheless, pushover plots in the Fig. 16 indicate that the lateral stiffness of HPR-TGF can be diversely shifted by applying various ρ factors. It is also notable that the formation of plastic hinges in columns of the HPR-TGF is postponed to significant lateral displacements beyond its target displacement ($\Delta_T = 0.594$ m). This is contrasted with the benchmark structure in which the first traces of column yielding are observed prior to reaching its target displacement ($\Delta_T = 0.792$m). Moreover, with reference to the Figs. 17(a) and (b), it is evident that in the both HPR-TGF and BRB-STMF structures no BRBs has yielded up to 0.1 m of the roof displacement. Afterward, the complete engagement of BRBs along the height of benchmark structure requires large displacements at its roof level ($\Delta_r = 0.5$ m), while for the HPR-TGF a marginal value of $\Delta_r = 0.14$ m is enough to get all BRBs yielded. This implies that the proposed energy based design approach has developed an accurate and efficient early-steps energy dissipating mechanism for the HPR-TGF systems.

4.7 Nonlinear time-history analysis results

The step by step dynamic response of HPR-TGF has been investigated through the time-history analysis. This

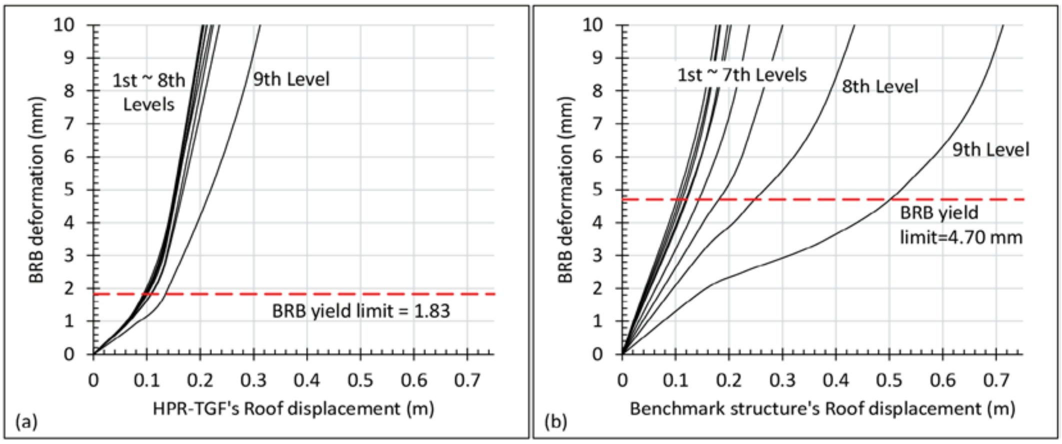

Fig. 17 BRB yielding sequence in the (a) HPR-TGF system; and (b) benchmark structure

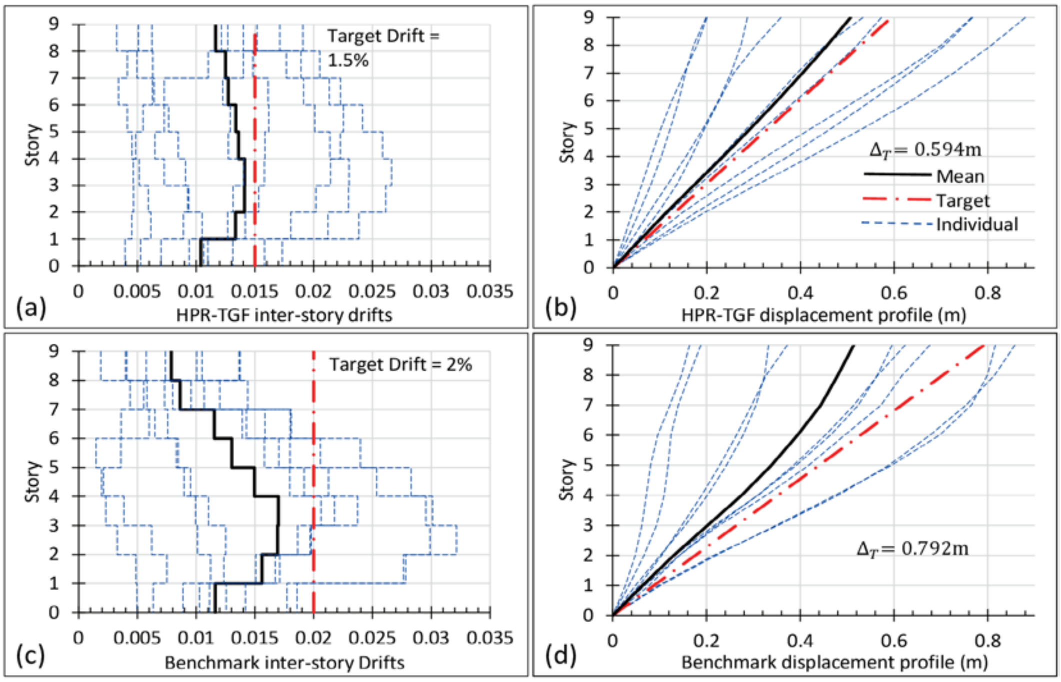

Fig. 18 Time-history analysis results: (a) inter-story drifts of the case study HPR-TGF; (b) Lateral displacement profile of the case study HPR-TGF; (c) inter-story drifts of the benchmark BRB-STMF; (d) Lateral displacement profile of the benchmark BRB-STMF

approach is performed using direct integration ($\gamma = 0.5$, $\beta = 0.25$) with Rayleigh damping to solve the corresponding vibrational equations. In the Rayleigh damping, as proposed by Clough and Penzien (1975), the mass proportional damping and the stiffness proportional damping are defined as functions of the mass matrix and the stiffness matrix scaled by coefficients of c_M and c_K, respectively. The estimation of these scale factors is based on the fundamental period of the building and also one of its post-elastic periods. This method is a common approach in the nonlinear time-history analysis to simulate the damping capacity of the whole system regardless of the additional damping due to the fluid viscous dampers. The FVDs are individually modeled as link elements. The output time steps of the analysis are evenly divided regarding the input time steps of the seismic records. However, the results of these analyses using the ground motions in the Table 2 are depicted in the Fig. 18. The case study HPR-TGF is intentionally designed to reach an average inter-story drift of $\theta_{AVG} = 1.29\%$ which is almost identical to the benchmark structure with $\theta_{AVG} = 1.3\%$. This is while in accordance to the Figs. 18(a) and (c), the target drift capacities for the case study HPR-TGF and the benchmark structure have been $\theta_c = 1.5\%$ and $\theta_c = 2\%$, respectively. Based on values of the deviation from target drift capacity which are $DTC = 24.25 \times 10^{-4}$ for the HPR-TGF and $DTC = 76.72 \times 10^{-4}$ for the benchmark structure, it is evident that the design procedure applied for HPR-TGFs is outperforming in comparison to that of the benchmark structure in terms of more accurate design results. Furthermore, by evaluating the lateral displacement profile of the HPR-TGF (Fig. 18(b)) versus the benchmark structure (Fig. 18(d)), the more uniform distribution of lateral strengths along the height of HPR-TGF and thus better formation of linear drift profile are obvious.

5. Conclusions

The main objective of this study is to modifying both truss girder frames and their design procedure in order to meet seismic demands properly. Therefore, a new configuration of truss girders which simultaneously accommodates varying types of energy dissipation devices is introduced. The proper functioning of these trusses has been evaluated and confirmed through the nonlinear finite element analysis. Then a pair of passive energy dissipating devices such as Buckling Restrained Braces (BRBs) and Fluid Viscous Dampers (FVDs) is implemented in each truss to form a Hybrid Passive Resistive Truss Girder Frame (HPR-TGF). The methodology for proper estimation of the seismic demands on various components of this framing system is extracted from the principles of the direct displacement based design approach. In this process, the overall energy dissipation capacity of the system is converted to an equivalent amount of viscous damping and then based on a displacement spectra the seismic demands are obtained. Afterward, the energy dissipation contribution of each structural component will be determined and the design process continues. This approach has been conducted for the proposed HPR-TGF system and the results are compared to those of a benchmark structure. Eventually, it is concluded that the ultimate behavior of the frame can be precisely described via the inelastic design parameters. However, it should be noted that achieving the design integrity in other HPR-TGFs with various heights or bay numbers requires an appropriate choice of inelastic design parameters which may be a field for further investigations.

References

Amiri, G.G., Shalmaee, M.M. and Namiranian, P. (2016), "Evaluation of a DDB design method for bridges isolated with triple pendulum bearings", *Struct. Eng. Mech.*, *Int. J.*, **59**(5), 803-820.

ANSYS version 5.4 [Computer Software], Houston, TX, USA.

ASCE7 (American Society of Civil Engineers) (2010), Minimum design loads for buildings and other structures; SEI/ASCE 7-10, Reston, VA, USA.

ASCE41 (American Society of Civil Engineers) (2006), Seismic rehabilitation of existing buildings; SEI/ASCE 41-06, Reston, VA, USA.

Basha, H. and Goel, S.C. (1995), "Special truss moment frames with Vierendeel middle panel", *J. Eng. Struct.*, **17**(5), 352-358.

Blandon, C.A. and Priestley, M.J.N. (2005), "Equivalent viscous damping equations for direct displacement based design", *J. Earthq. Eng.*, **9**(sup2), 257-278.

Chao, S.H. and Goel, S.C. (2008), "Performance-based plastic design of special truss moment frames", *Eng. J.-Am. Inst. Steel Constr. INC*, **45**(2), 127-150.

Chao, S.H. and Goel, S.C. and Lee, S.S. (2007), "A seismic design lateral force distribution based on inelastic state of structures", *Earthq. Spectra*, **23**(3), 547-569.

Clough, R. and Penzien, J. (1975), *Dynamics of Structures. International Student Edition*, McGraw-Hill Kogakusha, Ltd., Tokyo, Japan.

Constantinou, M.C., Soong, T.T. and Dargush, G.F. (1998), *Passive Energy Dissipation Systems For Structural Design and Retrofit*, Multidisciplinary Center for Earthquake Engineering Research Buffalo, NY, USA.

Della Corte, G. (2006), "Vibration mode vs. collapse mechanism control for steel frames", *Proceedings of the 4th International Specialty Conference on Behaviour of Steel Structures in Seismic Areas* (*STESSA 2006*), Yokohama, Japan.

Erfani, S., Babazadeh Naseri, A. and Akrami, V. (2012), "The beneficial effects of beam web opening in seismic behavior of steel moment frames", *Steel Compos. Struct.*, *Int. J.*, **13**(1), 35-46.

Fajfar, P. and Krawinkler, H. (1997), "Seismic Design Methodologies for the Next Generation of Codes", in *Proceedings of the International Workshop on Seismic Design Methodologies for the Next Generation of Codes*, Slovenia, June.

Goel, S.C. and Itani, A. (1994a), "Seismic Behavior of Open Web Truss Moment Frames", *J. Struct. Eng.*, **120**(6), 1763-1780.

Goel, S.C. and Itani, A. (1994b), "Seismic Resistant Special Truss Moment Frames", *J. Struct. Eng.*, **120**(6), 1781-1797.

Heidari, A. and Gharehbaghi, S. (2015), "Seismic performance improvement of Special Truss Moment Frames using damage and energy concepts", *Earthq. Eng. Struct. Dyn.*, **44**(7), 1055-1073.

Jacobsen, L.S. (1930), "Steady forced vibration as influenced by damping", *Transactions of ASME*, **52**(15), 169-181.

Kim, J., Lee, J. and Kang, H. (2016), "Seismic retrofit of special truss moment frames using viscous dampers", *J. Constr. Steel Res.*, **123**, 53-67.

Lee, D. and Taylor, D.P. (2001), "Viscous damper development and future trends", *Struct. Des. Tall Build.*, **10**(5), 311-320.

Leelataviwat, S. and Goel, S.C. and Stojadinovic, B. (1999), "Toward performance-based seismic design of structures", *Earthq. Spectra*, **15**(3), 435-461.

Magar Patil, H.R. and Jangid, R.S. (2015), "Numerical study of seismic performance of steel moment-resisting frame with buckling-restrained brace and viscous fluid damper", *IES J. Part A*: *Civil Struct. Eng.*, **8**(3), 165-174.

Maley, T.J., Sullivan, T.J. and Della Corte, G. (2010), "Development of a displacement-based design method for steel dual systems with buckling-restrained braces and moment-resisting frames", *J. Earthq. Eng.*, **14**(S1), 106-140.

Mazzolani, F. and Piluso, V. (1996), *Theory and Design of Seismic Resistant Steel Frames*, CRC Press.

Mohammadi, R.K. and Sharghi, A.H. (2014), "On the optimum performance-based design of eccentrically braced frames", *Steel Compos. Struct.*, *Int. J.*, **16**(4), 357-374.

PEER, NGA-WEST2 ground motion database (2016), http://ngawest2.berkeley.edu; University of California, Berkeley, CA, USA.

Pekcan, G., Linke, C. and Itani, A. (2009), "Damage avoidance design of special truss moment frames with energy dissipating devices", *J. Constr. Steel Res.*, **65**(6), 1374-1384.

Priestley, M.J.N. (1993), "Myths and fallacies in earthquake Engineering—conflicts between design and reality", *Bull. New Zealand Soc. Earthq. Eng.*, **26**(3), 329-341.

Priestley, M.J.N., Calvi, G.M. and Kowalski M.J. (2007), *Displacement Based Seismic Design of Structures*, IUSS Press, Pavia, Italy.

Salawdeh, S. and Goggins, J. (2016a), "Direct displacement based seismic design for single storey steel concentrically braced

frames", *Earthq. Struct., Int. J.*, **10**(5), 1125-1141.
Salawdeh, S. and Goggins, J. (2016b), "Performance based design approach for multi-storey concentrically braced steel frames", *Steel Compos. Struct., Int. J.*, **20**(4), 749-776.
SAP2000 (2015), CSI Analysis Reference Manual; Computers & Structures, Univ. Ave. Berkeley, CA, USA.
Shibata, A. and Sozen, M. (1976), "Substitute-structure method for seismic design in reinforced concrete", *ASCE J. Struct. Eng.*, **102**(1), 1-18.
Tecchio, G., Dona, M. and Modena, C. (2015), "Direct displacement-based design accuracy prediction for single-column RC bridge bents", *Earthq. Struct., Int. J.*, **9**(3), 455-480.
Tsai, K.C., Weng, Y.T., Lin, M.L., Chen, C.H., Lai, J.W. and Hsiao, P.C. (2003), "Pseudo Dynamic Tests of a Full Scale CFT-BRB Composite Frame: Displacement Based Seismic Design and Performance Evaluations", *Proceedings of the International Workshop on Steel and Concrete Composite Constructions, National Center for Research on Earthquake Engineering,* Taipei, Taiwan.
Wongpakdee, N., Leelataviwat, S., Goel, S.C. and Liao, W. (2014), "Performance-based design and collapse evaluation of buckling restrained knee braced truss moment frames", *J. Eng. Struct.*, **60**, 23-31.

CC